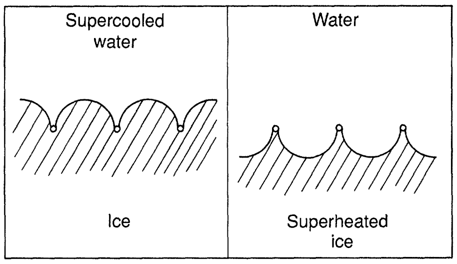

Fig. 5. Simple model of melting and freezing inhibition operating through the Kelvin effect—the influence of surface curvature upon melting point. The local radius of curvature needed to shift the melting point up or down by 1°C is about 175 Å if the surface energy is taken to be 20 ergs cm^{-2} and the geometry is idealized as two dimensional. The third dimension is important in the real case.

tion of the characteristics of the growth pits on the basal face of ice that form during growth within the freezing hysteresis gap (*8*). As far as the pits are concerned, this is freezing at a concave ice surface.

The mechanism of action of AFGPs and AFPs (antifreeze peptides) is under active study at present (*1*, *9–11*), and it is of interest that one of them inhibits melting in a way at least roughly symmetrical to its freezing inhibition. Probably the others do as well, although many of them may adsorb preferentially at interface orientations different from that of *D. mawsoni* (*12*). One can imagine two ways in which the AF molecules can adhere tightly enough to the ice-water interface to prevent growth or melting. One is ordinary adsorption, in which the linear or helical (*11*) molecules lie flat on the surface and bond to the ice, presumably fitting the ice surface structure (*1*), and the other would require some ice growth to engulf part of an AF molecule inside the ice crystal itself. Further ice growth might then be inhibited if there is a high free energy barrier against the rest of the molecule becoming buried within the crystal. These melting inhibition results argue against the need for partial engulfment and support of the idea of ordinary adsorption and the use of the phrase "adsorption inhibition" (*2*) for the antifreeze effect. (In fact, deciding this issue was the original motivation for this work.)

A two-dimensional representation of a simple, hypothetical mechanism for both freezing and melting inhibition by adsorption is shown in Fig. 5. It requires the adsorbed molecules to be bonded onto the ice-water interface very tightly and operates through the Kelvin effect. During either melting or freezing, the interface has to assume a radius of curvature before it can move past the originally adsorbed molecules and leave them completely within the liquid or the crystal. This radius of curvature dictates the supercooling or superheating required for motion of such an interface. The original hypothesis for freezing inhibition (*2*) involved the adsorbed molecules interfering with step passage, and is also, in principle, applicable to melting.

REFERENCES AND NOTES

1. A. L. DeVries, *Philos. Trans. R. Soc. London Ser. B* **304**, 165 (1984).
2. J. A. Raymond and A. L. DeVries, *Proc. Natl. Acad. Sci. U.S.A.* **74**, 2589 (1977).
3. W. B. Hillig, in *Growth and Perfection of Crystals*, R. H. Doremus, B. W. Roberts, D. Turnbull, Eds. (Wiley, New York, 1958), pp. 349–359.
4. C. A. Knight, *Nature* **220**, 62 (1968).
5. B. Kamb, *Science* **169**, 1343 (1970).
6. We learn from F. C. Frank that he was shown a demonstration of crystal superheating by G. Sears. Heat was fed into a flat face of a thin, perfect crystal—probably of salol—and melting occurred only at the edges.
7. F. C. Frank, in *Growth and Perfection of Crystals*, R. H. Doremus, B. W. Roberts, D. Turnbull, Eds. (Wiley, New York, 1958), pp. 411–418; F. C. Frank, *Z. Phys. Chem. Neue Folge* 77, 84 (1972); C. A. Knight and N. C. Knight, *Science* **150**, 1819 (1965); C. A. Knight, *J. Appl. Meteorol.* **5**, 710 (1966).
8. J. A. Raymond, P. Wilson, A. L. DeVries, *Proc. Natl. Acad. Sci. U.S.A.* **86**, 881 (1989).
9. A. L. DeVries, in *Animals and Environmental Fitness*, R. Gilles, Ed. (Pergamon, Oxford, 1980), pp. 583–607.
10. R. E. Feeney and Y. Yeh, *Adv. Protein Chem.* **32**, 191 (1978).
11. D. S. C. Yang, *et al.*, *Nature* **333**, 232 (1988).
12. C. A. Knight and A. L. DeVries, in *Atmospheric Aerosols and Nucleation*, P. E. Wagner and G. Vali, Eds. (Springer-Verlag, Berlin, 1988), pp. 717–720. Our unpublished work suggests that the adsorption plane for *D. mawsoni* AFGP is a high-index one near the prism plane, $(72\bar{9}0)$.

13. We thank C. DeVries for helpful criticism of the manuscript. The National Center for Atmospheric Research is sponsored by the National Science Foundation. Supported in part under NSF DPP grant 87-16296 to A.L.D.

20 March 1989; accepted 8 June 1989

Disorder-to-Order Transition in Settling Suspensions of Colloidal Silica: X-ray Measurements

K. E. Davis, W. B. Russel, W. J. Glantschnig

Dispersions of colloidal particles exhibit thermodynamic properties similar to those of molecular systems, including a hard sphere disorder-to-order transition. In experiments with organophilic silica in cyclohexane, gravity settling was used to concentrate the particles. With small particles the slow sedimentation permits rearrangement into the iridescent ordered phase, but larger particles form amorphous sediments instead. Scanning electron microscopy of the crystalline sediment indicates hexagonally close-packed layers. X-ray attenuation measurements reveal a discontinuity coincident with the observed boundary between iridescent and opaque regions. Sediments accumulating faster than the maximum rate of crystallization produce a glass, in accord with the classical theory for crystal growth.

SEDIMENTATION PROVIDES A MECHANISM for concentrating a dilute dispersion, forming a dense sediment on the bottom and clear liquid above. However, colloidal particles also execute Brownian motion and hence share many dynamic and thermodynamic properties with molecular systems, except with much longer relaxation times. For example, colloids diffuse down gradients in chemical potential and exhibit disorder-to-order transitions at high solid volume fractions. Thus the nominally simple sedimentation process actually couples gravity settling, diffusion, and crystallization in a highly nonideal system.

For hard spheres, the simplest of systems, short-range correlations characterize the disordered fluid state at volume fractions $\phi < 0.50$. However, both molecular dynamics simulations (*1*) and density functional theories (*2*) predict an ordered equilibrium state at higher volume fractions. Thus a hard sphere system at $\phi > 0.50$ should rearrange spontaneously, as a result of Brownian motion, from an initially disordered state into the equilibrium ordered state.

Indeed, Hachisu and Kobayashi (*3*) detected coexisting disordered and ordered phases, with $\phi = 0.50$ and 0.55, respectively, for aqueous polymer lattices at ionic strengths high enough to screen electrostatic repulsions. Recently, Pusey and van Megen (*4*, *5*) observed the transition for polymethylmethacrylate spheres at $0.56 > \phi \geq 0.50$ in a nonaqueous solvent but glasses at higher ϕ where the low mobility of the spheres apparently suppresses the rearrangement (*6*). Our experiments were designed to monitor crystallization during sedimentation and thereby provide information on the dynamics of the crystallization process.

K. E. Davis and W. B. Russel, Department of Chemical Engineering, Princeton University, Princeton, NJ 08544.
W. J. Glantschnig, AT&T Engineering Research Center, Post Office Box 900, Princeton, NJ 08540.

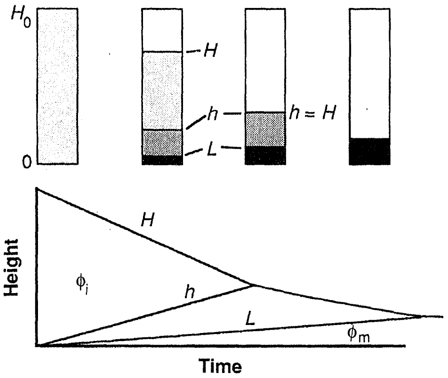

Fig. 1. Schematic of the settling process illustrating the development of the regions of clear fluid, $H < x < H_0$; uniform dispersion, $h < x < H$; fan, $L < x < h$; and sediment, $0 < x < L$.

Silica spheres were synthesized by the method of Stöber *et al.* (*7*) and then stabilized by surface esterification with 1-octadecanol according to the procedure of van Helden *et al.* (*8*). The resulting particles are easily dispersed in cyclohexane, whose low dielectric constant eliminates electrical charges and whose nearly identical refractive index suppresses van der Waals forces. Therefore, the particles behave as hard spheres (*9*) and are sufficiently transparent to allow visual observation of the bulk dispersion. Batches with diameters of $2a$ = 0.20, 0.31, 0.34, and 0.43 μm, as determined from their settling velocities, and standard deviations of less than 6%, determined by electron microscopy, were prepared in this way.

In our experiments with uniform initial volume fractions $0.04 < \phi_0 < 0.30$ sedimentation proceeds as illustrated in Fig. 1. The discontinuity at the top, $H(t)$, where t is time, falls at the settling velocity $U(\phi_0)$ of particles in the uniform dispersion below. Two other visible discontinuities, $L(t)$ delimiting the top of the sediment and $h(t)$ marking the bottom of the uniform region, rise at constant velocities and define a region, known as the fan, in which the volume fraction increases smoothly with depth. The velocity dL/dt is independent of ϕ_0 and less than dh/dt, which increases with increasing ϕ_0. Eventually H and h converge and proceed downward but at a steadily decreasing rate. When the top of the suspension disappears into the sediment, the process is complete. The path of individual particles roughly parallels that of the discontinuity at the top. The diagram in the lower portion of Fig. 1 sketches the trajectory of each interface.

Figure 2 shows the lower portions of two dispersions containing particles 0.34 μm in diameter at two different initial volume fractions, $\phi_0 = 0.045$ on the left and $\phi_0 = 0.09$ on the right. After 220 hours of settling (Fig. 2A), the clear fluid remains out of view at the top but the hazy regions correspond to the uniform dispersion at the initial volume fraction and the opaque region immediately below comprises the fan. Both samples have accumulated sufficient sediment to undergo the phase transition as indicated by the bands of iridescence. The ordered packing diffracts white light into a spectrum of colors provided $\phi a^3 < 5\pi\ \mu m^3$ (*9, 10*), with the multiple facets indicating polycrystallinity. After 420 hours (Fig. 2*B*), settling is almost complete for the less concentrated sample, that is, $H = h \rightarrow L$. The iridescence begins later, higher in the sediment, for the sample with the higher initial volume fraction.

The sharp interface between the iridescent phase and the opaque region above signals a true phase transition separating the disordered fluid within the fan from the crystalline sediment below. The extent of the fan increases with increasing volume fraction, but the crystallization, once initiated, proceeds at the same rate in the two cases, limited by the kinematics of the settling process. The lower portions of the sediments contain small speckles of iridescence, suggesting homogeneous nucleation and growth of crystallites, but the long columnar crystals dominate Fig. 2, A and B. Ultimately both samples crystallize completely, except for 1 to 2 mm of an amorphous, glassy sediment at the bottom and a much thinner disordered layer at the top.

Scanning electron microscopy of the iridescent sediment (Fig. 3A) reveals planes of hexagonally packed, 0.31-μm spheres, arranged in either a face-centered cubic structure or randomly stacked layers. Figure 3B shows a side view of the sediment with the orientation preserved. Here the planes of hexagonal packing lie roughly perpendicular to the micrograph. Thus, settling particles find lattice sites on planar hexagonally close-packed layers that grow one dimensionally, that is, in the vertical direction.

Certain prominent features such as the sediment, the fan, and the top of the suspension are discernible to the naked eye, allowing one to track the stages of sedimentation without the aid of elaborate diagnostics. Accurate measurement of the volume fraction profiles, however, is considerably more complex. Our x-ray measurements take advantage of the attenuation of collimated electromagnetic radiation by matter through photon absorption and scattering events (*11*). Silica attenuates photons to a much greater extent than cyclohexane, so that particle volume fractions may be quantified by the fraction of radiation transmitted. An elemental lanthanum filter selects an intensity distribution with a sharp peak at 38 keV, and calibration against carefully prepared dispersions defines the attenuation coefficient as a linear function of the silica volume fraction. Because the volume fraction is uniform across any horizontal layer, we need data only as a function of vertical position.

Figure 4A displays a series of such volume fraction profiles plotted against height above the bottom at various times. The dispersion consists of the 0.31-μm particles at $\phi_0 = 0.18$ in a test tube 200 mm high and about 10 mm in diameter. The profiles above the sediment conform qualitatively with those expected from a purely kinematic model (*12*) incorporating hindered settling, that is, a sedimentation velocity decreasing with increasing volume fraction. However, diffusion is significant, smoothing the discontinuity at the top of the fan where $0.20 \leq \phi \leq 0.30$. The sediment, the region at the bottom with $\phi > 0.60$, grows with time and is gradually compressed to a maximum ϕ, $\phi_m \approx 0.66$ to 0.68, significantly above random close packing. The profiles for the time from 809 to 2931 hours display a steep gradient at the top of the sediment for $0.53 \leq \phi \leq 0.60$. This virtual discontinuity can persist only with a vanishing diffu-

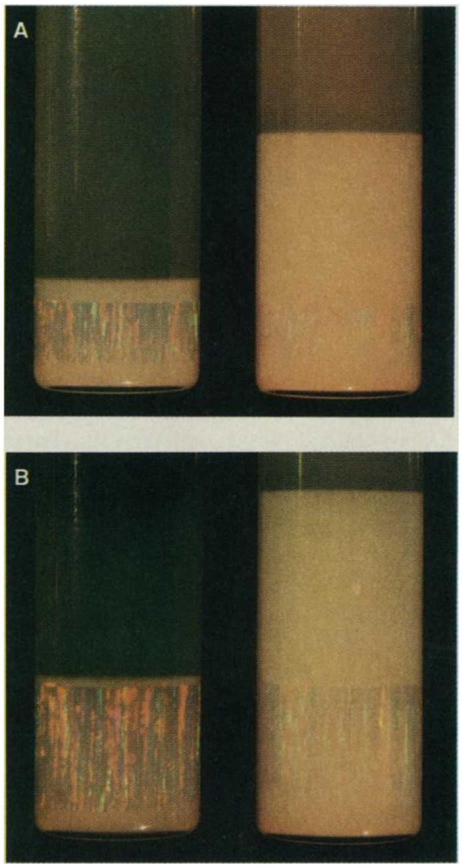

Fig. 2. Dispersions of silica spheres 0.34 μm in diameter in cyclohexane at initial volume fractions of 0.045 (left) and 0.09 (right) after settling for (**A**) 220 and (**B**) 420 hours in tubes approximately 10 mm in diameter.

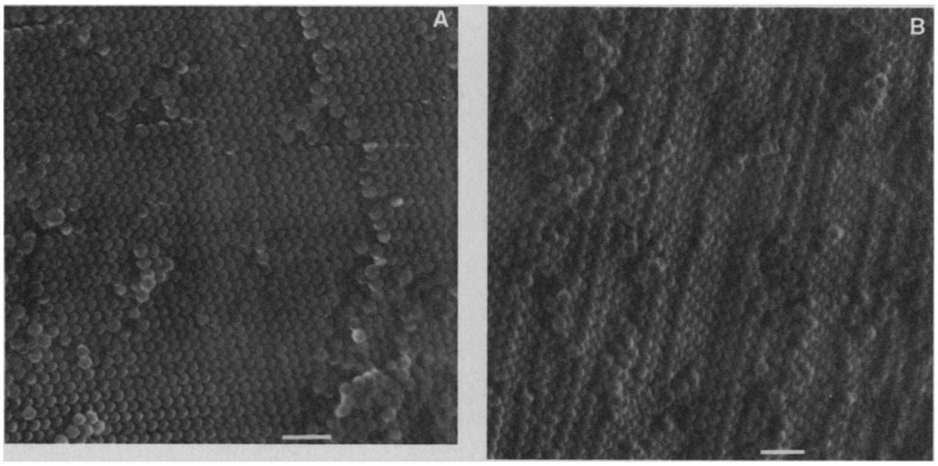

Fig. 3. Scanning electron micrograph of the iridescent sediment formed from silica spheres 0.31 μm in diameter, illustrating (**A**) the hexagonal close-packed symmetry of layers and (**B**) the appearance from the side with the orientation preserved, suggesting the origin of the vertical striations in Fig. 2. Scale bar = 1 μm.

sivity, that is, a chemical potential on the right side of the discontinuity equal to or greater than that on the left side, substantiating the presence of a phase transition.

Figure 4B illustrates the trajectory diagram for this sample. The solid lines represent the predictions of the Kynch theory (*12*) with $\phi_m = 0.68$ and

$$U(\phi) = (2a^2\ \Delta\rho g/9\nu)(1 - \phi)^6 \qquad (1)$$

where $\Delta\rho$ is the density difference, g is the gravitational acceleration, and ν is the fluid viscosity; the + symbols indicate the observed positions of the visible discontinuities, H, h, and L; the other symbols are from the x-ray measurements. The volume fraction contours within the fan propagate upward linearly from the bottom, with $\phi = 0.53$ lying just above the surface of the iridescent sediment, $L(t)$.

Similar experiments with 0.20-μm particles with $\phi_0 = 0.13$ and 0.14 were performed. Owing to the smaller particle size, these dispersions settle more slowly, are more transparent, and scatter predominantly blue light; nonetheless, both dispersions display the iridescence characteristic of ordered sediments with little evidence of an amorphous region at the bottom. Experiments with larger particles, $2a = 0.43$ μm, exhibit the same overall settling pattern but do not form crystalline sediments at similar initial volume fractions.

The volume fraction profiles from the x-ray measurements and the resulting trajectory diagrams suggest that crystallization occurs just above the sediment where particles have both the mobility and the thermodynamic driving force to rearrange into ordered domains. In the absence of crystallization, the $\phi = 0.50$ contour lies in the fan above the random close-packed sediment where $\phi = 0.63$. Within this range the rate of crystallization rises from zero at $\phi = 0.50$, passes through a maximum, and then falls back to zero as the particle mobility vanishes at random close packing. Only if the maximum rate of crystallization exceeds the rate of growth of an amorphous sediment does the phase transition occur. Otherwise the particles are compressed into a glassy state. Because the rate of sedimentation increases as the square of the diameter d^2 and the rate of crystallization decreases as d^{-2} (*13*), the range (factor of 2) of particle sizes studied here suffices to produce sediments ranging from completely crystallized to entirely amorphous.

Indeed, a quantitative application of classical theories for transient settling and one-dimensional crystal growth agrees with our results. The kinematic theory (*12*), applied to a dispersion of hard spheres settling according to Eq. 1, predicts that a disordered sediment at random close packing accumulates at a rate $0.057(2a^2\ \Delta\rho g/9\nu)$. The theory for one-dimensional crystal growth (*13*) assumes a rate of the form $(fD_s/a)[1 - \exp(\Delta\mu/kT)]$, where f is a proportionality constant, D_s is the self-diffusion coefficient, $\Delta\mu$ is the difference in chemical potential between the ordered and disordered phases, k is the Boltzmann constant, and T is the absolute temperature. With $\Delta\mu$ calculated from simulations for hard spheres (*1*) and

$$D_s = (kT/6\pi\ \nu\ a)(1 - \phi/0.63)^2 \qquad (2)$$

to reflect the vanishing mobility at random close packing, the growth rate attains a maximum value of $0.0085f(kT/6\pi\ \nu\ a^2)$. Hence, the crossover from crystalline to amorphous sediments, observed for $2a \approx 0.4$ μm, implies $f \approx 0.1$, in reasonable accord with simulations for molecular systems (*14*).

We have quantified the hard sphere, disorder-to-order transition in settling colloidal dispersions with particle sizes ranging from 0.20 to 0.34 μm. Initially too dilute to favor the ordered state, disordered dispersions settle into denser regions near the bottom. The close packing of particles in the sediment itself suppresses the transition kineti-

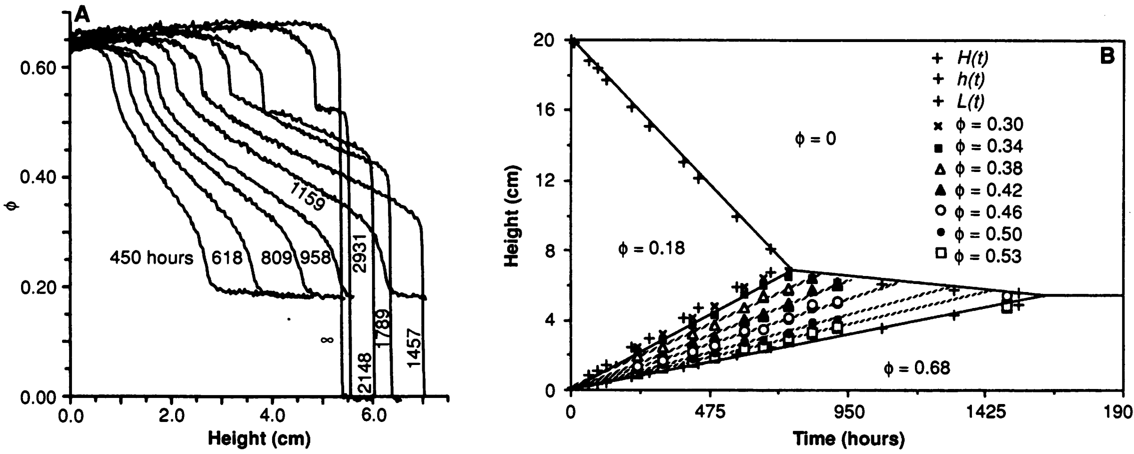

Fig. 4. (**A**) Volume fraction profiles obtained via x-ray attenuation for spheres 0.31 μm in diameter with $\phi_0 = 0.18$. The sediment corresponds to $0.60 < \phi < 0.68$, the disorder-to-order transition to $0.53 < \phi < 0.60$, and the fan to $0.30 < \phi < 0.53$. (**B**) Volume fraction contours derived from the data of (A), the observations of the discontinuities (+), and the kinematic theory (———, discontinuities; - - - -, contours).

cally, although it is favored thermodynamically. However, x-ray scanning reveals that the volume fraction in the fan above the sediment increases smoothly with depth, passing through the phase boundary at $\phi = 0.50$ while the particles remained dispersed. For the 0.31-μm particles at $\phi \approx 0.53$, the chemical potential of the disordered phase exceeds that of the ordered phase sufficiently to produce a crystallization rate equal to the kinematic velocity; hence, the transition produces a coexisting crystalline phase with $\phi \approx 0.60$. For the 0.43-μm particles, the maximum crystallization rate apparently falls below the growth rate of an amorphous sediment for the volume fractions reported here and crystallization does not occur. Thus, for these initial volume fractions there exists a maximum size above which particles settle too rapidly to find sites on a crystal lattice, resulting in amorphous sediments.

REFERENCES AND NOTES

1. L. V. Woodcock, *Ann. N.Y. Acad. Sci.* **37**, 274 (1981).
2. A. D. J. Haymet, *J. Chem. Phys.* **78**, 4641 (1983).
3. S. Hachisu and Y. Kobayashi, *J. Colloid Interface Sci.* **46**, 470 (1974).
4. P. N. Pusey and W. van Megen, *Nature* **320**, 340 (1986).
5. ——, *Phys. Rev. Lett.* **59**, 2083 (1987).
6. D. Frenkel and J. P. McTague, *Annu. Rev. Phys. Chem.* **31**, 491 (1980).
7. W. Stöber, A. Fink, E. Bohn, *J. Colloid Interface Sci.* **26**, 62 (1968).
8. A. K. van Helden *et al.*, *ibid.* **81**, 354 (1981).
9. C. G. de Kruif *et al.*, *J. Phys. (Paris)* **46**, 295 (1985).
10. P. Pieranski, *Contemp. Phys.* **24**, 25 (1983).
11. W. J. Glantschnig and A. Holliday, *Appl. Opt.* **26**, 983 (1987).
12. G. J. Kynch, *Trans. Faraday Soc.* **48**, 166 (1952).
13. K. E. Davis and W. B. Russel, *Adv. Ceramics* **21**, 573 (1987).
14. J. Q. Broughton *et al.*, *Phys. Rev. Lett.* **49**, 1496 (1982).

15. We are indebted to C. W. Draper for support of this research and to K. D. Pohl who handled much of the x-ray measurements. This work was performed under Department of Energy Office of Basic Energy Sciences grant DE-FG02-85ER45210.

6 March 1989; accepted 5 May 1989

Hydrophobic Organization of Membrane Proteins

D. C. Rees,* L. DeAntonio, D. Eisenberg

Membrane-exposed residues are more hydrophobic than buried interior residues in the transmembrane regions of the photosynthetic reaction center from *Rhodobacter sphaeroides*. This hydrophobic organization is opposite to that of water-soluble proteins. The relative polarities of interior and surface residues of membrane and water soluble proteins are not simply reversed, however. The hydrophobicities of interior residues of both membrane and water-soluble proteins are comparable, whereas the bilayer-exposed residues of membrane proteins are more hydrophobic than the interior residues, and the aqueous-exposed residues of water-soluble proteins are more hydrophilic than the interior residues. A method of sequence analysis is described, based on the periodicity of residue replacement in homologous sequences, that extends conclusions derived from the known atomic structure of the reaction center to the more extensive database of putative transmembrane helical sequences.

THREE-DIMENSIONAL PROTEIN structures reflect a favorable energetic balance between protein-protein and protein-solvent interactions. For water-soluble proteins, polar and charged residues are often on the surface, whereas apolar residues tend to occur in the interior (*1–6*). The hydrophobic organization of membrane proteins is less well understood, although models of membrane protein structures (*7, 8*) make use of the hydrophobic transmembrane α helix and an "inside-out" pattern of residue hydrophobicity in which the interior residues are more polar than the membrane-exposed surface residues (*9*). The availability of atomic structures for bacterial photosynthetic reaction centers (RCs) (*10–12*) allows a more quantitative analysis of the hydrophobic organization of a membrane protein. The results of this analysis are described for the RC from *Rhodobacter sphaeroides*. Based on these observations, a method of analysis of homologous sequences is proposed that may be generally useful in assigning interior and surface (membrane-exposed) residues of transmembrane helices from sequence information. Application of this method to a variety of membrane-protein families is described.

The RCs from purple bacteria consist of three membrane-bound subunits, containing a total of 11 transmembrane α helices. The position in the membrane of the RC from *Rb. sphaeroides* was proposed (*13*) with the use of a hydrophobic free energy function (*14*) to establish the orientation of most favorable interaction between the RC and a nonaqueous phase. Amino acids located in the nonpolar region of the membrane were assigned (*13*) to one of three classes: buried, semi-exposed, and exposed residues, which were defined as having >80%, 50 to 80%, and <50%, respectively, of their accessible surface area in an isolated helix buried upon association of that helix in the RC structure. The average residue hydrophobicity in each class, $\langle h \rangle$, may be determined from the amino acid composition of each class, combined with a measure of the hydrophobicity of each residue, from the relation:

$$\langle h \rangle = \Sigma c_i h_i \qquad (1)$$

where c_i is the molar fraction of the ith amino acid in a particular class, h_i is the residue hydrophobicity, and the sum is over all 20 amino acids. Values for h_i are assigned from the consensus hydrophobicity scale of Eisenberg *et al.* (*15*). The average residue hydrophobicities for the buried, semi-exposed, and exposed classes are 0.19, 0.31, and 0.48, respectively (Table 1). Increasing apolarity is associated with more positive hydrophobicity values, so that buried residues in the membrane-spanning region of the RC are less hydrophobic than exposed residues. The greater hydrophobicity of exposed residues of the membrane-spanning helices in the RC structure is not sensitive to the precise definition of exposed and buried. Chothia (*4*) defined buried residues in water-soluble proteins as those having <5% of their surface accessible to solvent. With this criterion, average residue hydrophobicities

Table 1. Mean residue hydrophobicities for buried and exposed residues.

Protein types	Mean residue hydrophobicities	
	Buried	Exposed
	Transmembrane proteins	
11 RC helices	0.19*	0.48
11 RC helices	0.22†	0.36
35 Helices (Table 2)	0.15‡	0.34
	Water-soluble proteins	
37 Monomers	0.24†	−0.25
23 Oligomers	0.19†	−0.28
7 Hemoglobin helices	0.17‡	−0.26

Definition of buried residues: *>80% area buried in helices (*13*); †<5% residue area exposed (*4*). ‡Hydrophobic moment (*25*).

Department of Chemistry and Biochemistry, Molecular Biology Institute, University of California, Los Angeles, Los Angeles, CA 90024.

*To whom correspondence should be sent at Division of Chemistry and Chemical Engineering 147-75 CH, California Institute of Technology, Pasadena, CA 91125.